



Chapter 15

Structural Damage Identification for Plate-Like Structures Using Two-Dimensional Teager Energy Operator-Wavelet Transform

Wei Zhou, Yongfeng Xu, and Jueseok Kim

Abstract Waveforms of propagating flexural waves can reveal plentiful information about anomalies caused by damage-wave interactions, and such anomalies can be used for damage identification. However, they can be masked by the interference of measurement noise and may be able to indicate only a fraction of the extent of the damage. In this paper, an effective noise-robust damage identification method is proposed. It extracts local anomalies based on two-dimensional curvature propagating flexural waves (2D-CPFW). To alleviate adverse effects of measurement noise on calculating 2D-CPFW, the continuous wavelet transform with a second-order Gaussian function is used as a differentiation operator. Three two-dimensional quantities, including the curvature of the 2D-CPFW, Teager energy of 2D-CPFW, and Teager energy of the curvature of the 2D-CPFW, are defined and they can intensify local anomalies caused by the existence of damage. To obtain a complete identification of damage extent based on the anomalies, a two-dimensional accumulative damage index is defined. A convergence index is introduced to determine the number of waveforms to be included when calculating the damage index. Effectiveness and noise-robustness of the proposed method are investigated in a numerical example of a damaged plate. Results verify that the proposed method is effective and noise-robust in identifying the location and extent of damage.

Keywords Baseline-free structural damage identification · Teager energy operator · Curvature propagating flexural waves · Continuous wavelet transform

15.1 Introduction

Structures in service for mechanical, aerospace, and civil engineering purposes can suffer from aging and deterioration due to long-term environmental effects and operational loads. To avoid catastrophic structural failures, structural health monitoring is critical by identifying existing developing deterioration and assessing their conditions [1–3]. Vibration-based damage identification has been a main research topic of structural dynamics for structural health monitoring in recent decades. Quantitative changes in local stiffness and/or mass can occur when local damage exists in a structure [4–7]. Hence, vibration characteristics of the structure, such as natural frequencies, operating deflection shapes, and mode shapes, can be used for damage identification. The natural frequencies-based methods are generally used for global identification, as they can be estimated with excitation and response points that are away from the damage [8]. Adams et al. [9] found that a damage state of a structure can be identified as reduction in stiffness, which leads to changes of its natural frequencies. A damage identification technique based on changes of natural frequencies was investigated by comparing natural frequencies at pristine and damage states [10]. The mode shapes and operating deflection shapes-based methods are considered local identification, as local anomalies cannot be identified unless the locality of the anomalies falls within a measurement grid [8]. Besides, mode shapes and operating deflection shapes-based methods are vulnerable to measurement noise and only relatively large damage is identifiable by using local anomalies in mode shapes and operating deflection shapes [11]. The use of curvatures of mode shapes and operating deflection shapes, referred to as curvature mode shapes and curvature operating deflection shapes, respectively, for damage identification were proposed in Refs. [12] and [13], respectively. It was shown that curvature mode shapes and curvature operating deflection shapes are more sensitive to small damage than mode shapes and operating deflection shapes. One the other hand, uses of continuous wavelet transforms (CWTs) were proposed and investigated in

W. Zhou · Y. Xu (✉) · J. Kim

Department of Mechanical and Materials Engineering, University of Cincinnati, Cincinnati, OH, USA

e-mail: zhouw6@mail.uc.edu; xu2yf@uc.edu; kim5jk@mail.uc.edu

Refs. [14–17] to accurately calculate the curvature mode shapes. The multi-scale property of CWT can smooth measurement noise and minimize errors by increasing the value of its scale parameter. However, global fluctuation of trends in curvature mode shapes and curvature operating deflection shapes can mask their local anomalies caused by damage. To address this problem, Teager energy operator (TEO) has been applied to further intensify local anomalies for damage identification based on curvature mode shapes calculated by CWT [18, 19]. TEO can intensify local anomalies and minimize global fluctuation of trends. Its use was introduced by combining CWT for identification of multiple damage for beams in Ref. [18]. Two-dimensional TEO was applied to intensify local anomalies of two-dimensional curvature mode shapes calculated by CWT for plates-like structures [19].

Besides vibration characteristics, propagating elastic waves can reveal local anomalies that exist in the neighborhood of damage and assist with its identification by capturing and visualizing anomalies of waves. Propagating elastic waves-based methods have been investigated and applied for damage identification in recent decades. Frequency-wavenumber domain analysis is one of the wave-based methods. It is capable of eliminating the incident waves and separating wave modes to highlight the presence of any reflected waves associated with damage. Ruzzene [20] introduced the frequency-wavenumber domain analysis for damage identification by using waveforms obtained by a scanning laser Doppler vibrometer (SLDV). Kudela et al. [21] introduced an adaptive wavenumber filtering technique by constructing a filter mask in the wavenumber domain to solve an issue caused by boundary reflections of propagating waves. Wave spectra in the frequency-wavenumber domain can show distinction among wave modes, but the space information is lost in the analysis. Hence, a short-space two-dimensional Fourier transform was introduced in Ref. [22], which yields the frequency-wavenumber spectra at various spatial locations. Besides, the waveform analysis was studied for damage identification purposes. It extracts local anomalies in waveforms of the propagating waves for damage identification. The waveform analysis was introduced in Ref. [23]: waveforms were measured by an SLDV and root mean square values of their complete time history were used to formulate a damage index. An integral mean value damage index was introduced in Ref. [24] and compared with the damage index based on root mean square values. It was shown that the damage index based on root mean square values is more sensitive to the existence of damage and less sensitive to that of environmental noise. To improve the sensitivity of waveform analysis for damage identification, new waveform analyses were recently presented based on curvatures of the waveforms. The reason is that curvature mode shapes have proved more damage-sensitive than mode shapes and used for damage identification. Sha et al. [25] introduced a concept of wavefield curvature by calculating curvatures of waveforms of propagating waves at selected time instants, and an energy image was then formed by square sums of the curvatures of waveforms of the propagating waves. Xu et al. [8] presented curvature of waveforms of propagating flexural waves by using local-regression polynomials to estimate curvature waveforms of a pseudo-pristine structure.

In this work, a baseline-free structural damage identification method is proposed for plate-like structures. It identifies location and extent of damage based on two-dimensional curvature propagating flexural waves (2D-CPFW). The 2D-CPFW is analogous to two-dimensional curvature mode shapes in Ref. [19]. A two-dimensional CWT is used to calculate 2D-CPFW for alleviating adverse effects of measurement noise and errors. To further intensify local anomalies based on the 2D-CPFW, three quantities are defined, including the curvature of the 2D-CPFW, Teager energy of the 2D-CPFW, and Teager energy of the curvature of the 2D-CPFW. A damage index is proposed to identify damage based on the three defined quantities. In the process of calculating the damage index, a convergence index is introduced to determine the number of waveforms to be included. Numerical investigations are conducted to study the effectiveness and noise-robustness of the proposed method.

The rest of the paper is arranged as follows. In Sect. 15.2, the proposed damage identification method based on 2D-CPFW is presented. In Sect. 15.3, the numerical investigations are described, respectively. Conclusions of this work are presented in Sect. 15.4.

15.2 Methodology

15.2.1 Formulation of 2D-CPFW for Plate-Like Structures

A propagating flexural wave of a plate-like structure can be considered as a three-dimensional spatial-temporal signal, as it consists of two-dimensional waveforms at different time instants denoted by t . A waveform of the propagating flexural wave at t , denoted by $W_t(x, y)$, can be considered as an instantaneous deformation with x and y being the spatial coordinates of a point on the structure. The mean curvature of $W_t(x, y)$ is the second-order spatial differentiation of $W_t(x, y)$, and it can be expressed by Yoon et al. [26]

$$\kappa_t^{2D} = \kappa_{x,t} + \kappa_{y,t} = \frac{\partial^2 W_t(x, y)}{\partial x^2} + \frac{\partial^2 W_t(x, y)}{\partial y^2} = \nabla^2 W_t(x, y) \quad (15.1)$$

where

$$\begin{cases} \kappa_{x,t} = \frac{\partial^2 W_t(x, y)}{\partial x^2} \\ \kappa_{y,t} = \frac{\partial^2 W_t(x, y)}{\partial y^2} \end{cases} \quad (15.2)$$

denote curvature propagating flexural waves along x - and y -axes, respectively, and ∇^2 is the Laplace operator. The instantaneous bending moments of the plate at a spatial point along x - and y -axes, denoted by $M_{x,t}$ and $M_{y,t}$, respectively, can be calculated by

$$M_{x,t}(x, y) = -D(x, y)(\kappa_{x,t} + \nu\kappa_{y,t}) \quad (15.3)$$

and

$$M_{y,t}(x, y) = -D(x, y)(\kappa_{y,t} + \nu\kappa_{x,t}) \quad (15.4)$$

respectively, where

$$D = \frac{Eh^3}{12(1-\nu^2)} \quad (15.5)$$

is the flexural rigidity of the structure, in which E and ν denote the Young's modulus and Poisson's ratio, respectively, and h denotes the thickness of the structure. Summing up Eqs. (15.3) and (15.4) yields

$$M_{x,t}(x, y) + M_{y,t}(x, y) = -D(x, y)(\kappa_{x,t} + \nu\kappa_{y,t} + \kappa_{y,t} + \nu\kappa_{x,t}) = -D(x, y)(1+\nu)(\kappa_{x,t} + \kappa_{y,t}) \quad (15.6)$$

Rearranging Eq. (15.6) and applying Eq. (15.1) yield

$$\kappa_t^{2D} = \kappa_{x,t} + \kappa_{y,t} = -\frac{M_{x,t}(x, y) + M_{y,t}(x, y)}{D(x, y)(1+\nu)} \quad (15.7)$$

When small-extent damage occurs to the structure, the value of D will change in the neighborhood of the damage. More importantly, local anomalies occur to κ_t^{2D} and can be used to reveal the existence of the damage. An instantaneous mean curvature κ_t^{2D} can be obtained using the second-order central finite difference scheme [26]. However, the scheme can amplify adverse effects of measurement noise and errors in $W_t(x, y)$. It is proposed that CWT with the second-order Gaussian function be used as the second-order differentiation operator for calculating κ_t^{2D} as it can alleviate the adverse effects of measurement noise and errors [19]. The differentiation can be achieved by a convolution of $\nabla^2 W_t(x, y)$ in Eq. (15.1) with a zeroth-order Gaussian wavelet function:

$$g_{u,v,s}(x, y) = \frac{1}{\sqrt{\pi}s} e^{-\left(\left(\frac{x-u}{s}\right)^2 + \left(\frac{y-v}{s}\right)^2\right)} \quad (15.8)$$

where s is the scale parameter, and u and v are translation parameters along x - and y -axes, respectively. The convolution is denoted by $\nabla^2 W_t \otimes g_{u,v,s}$ with \otimes being the notation of convolution. Based on the differentiation property of the convolution [27], the following relationship exists:

$$\nabla^2 W_t \otimes g_{u,v,s} = W_t \otimes \nabla^2 g_{u,v,s} \quad (15.9)$$

where $\nabla^2 g_{u,v,s}$ calculates the second-order Gaussian function, which is often referred to as the Mexican hat wavelet function. The term $W_t \otimes \nabla^2 g_{u,v,s}$ in Eq. (15.9) is defined as the 2D-CPFW, and it can be further expressed by

$$\begin{aligned}
W_{s,t}''(u, v) &= W_t \otimes \nabla^2 g_{u,v,s} \\
&= \frac{1}{\sqrt{\pi}s} W_t \otimes \nabla^2 e^{-\left(\left(\frac{x-u}{s}\right)^2 + \left(\frac{y-v}{s}\right)^2\right)} \\
&= s^2 \nabla^2 \int_{-\infty}^{\infty} \int_{-\infty}^{\infty} W_t(x, y) \frac{1}{\sqrt{\pi}s} e^{-\left(\left(\frac{x-u}{s}\right)^2 + \left(\frac{y-v}{s}\right)^2\right)} dx dy \\
&= s^2 \nabla^2 (W_t \otimes g_{u,v,s})
\end{aligned} \tag{15.10}$$

It is indicated by Eq. (15.10) that the calculation of $W_{s,t}''(u, v)$ is equivalent to an application of ∇^2 to $W_t \otimes g_{u,v,s}$. While the level of the measurement noise and errors in W_t can be lowered by its convolution with $g_{u,v,s}$, which acts as a low-pass filter, the application of ∇^2 will not suffer from the amplified adverse effects of the measurement noise and errors that exist in that of a finite difference scheme.

15.2.2 Local Anomalies Intensified from $W_{s,t}''$

Though local anomalies caused by damage in W_t can be identified in $W_{s,t}''$, they can be masked by global trends of $W_{s,t}''$, similar to those in curvature mode shapes [28, 29]. Hence, a high-order derivative of $W_{s,t}''$ and their Teager energy [19, 30] can be used to further intensify the local anomalies from the trends and identify the location of damage by minimizing the global trends.

Curvature of $W_{s,t}''$

Based on the differentiation property of CWT and Eq. (15.9), the r th-order derivative $W_{s,t}''$ using CWT is expressed by

$$W_{s,t}^{(r+2)} = \nabla^r (W_{s,t}'' \otimes g_{u,v,s}) = W_{s,t}'' \otimes \nabla^r g_{u,v,s} = W_{s,t} \otimes \nabla^{r+2} g_{u,v,s} \tag{15.11}$$

and it calculates CWT of W_t with the $(r+2)$ th-order Gaussian wavelet function. It is shown that CWT of a mode shape with the 4th-order Gaussian wavelet function is capable of localizing damage and the use of a higher-order Gaussian wavelet function can become necessary for a high-order mode shape [31]. The reason is that the high-order mode shape cannot be well fitted by a 4th-order polynomial. In practice, a dense measurement grid is applied for measuring W_t to avoid spatial aliasing, which is also the case in this work. Further, the width of an interval of non-zero values of $g_{u,v,s}$ depends on the value of s : the smaller s , the smaller the interval. In a small interval, the measured W_t can be well fitted by a 4th-order polynomial, and hence the proper value of r in Eq. (15.11) is chosen to be 2. In other words, CWT of W_t with the 4th-order Gaussian wavelet function can be used to intensify local anomalies for damage identification purposes. When $r = 2$, Eq. (15.11) can be written as

$$W_{s,t}^{(4)} = W_{s,t} \otimes \nabla^4 g_{u,v,s} = s^2 \nabla^4 (W_t \otimes g_{u,v,s}) \tag{15.12}$$

and $W_{s,t}^{(4)}$ is called the curvature of $W_{s,t}''$.

Local Anomalies Intensification Using TEO

TEO was first proposed to estimate the point-wise energy of a one-dimensional oscillating discrete signal $p[n]$ with n denoting the number of a discrete signal value. It is a nonlinear operator and can be expressed by Kaiser [32]

$$\Psi(p[n]) = p^2[n] - p[n-1]p[n+1] \tag{15.13}$$

Later, the TEO was extended to handle a two-dimensional discrete signal $q[n, m]$ with $[n, m]$ denoting the discrete number of a discrete signal value [33], and the two-dimensional TEO can be expressed by

$$\begin{aligned}\Psi^{2D}(q[n, m]) &= q^2[n, m] - q[n-1, m]q[n+1, m] + q^2[n, m] - q[n, m-1]q[n, m+1] \\ &= 2q^2[n, m] - q[n-1, m]q[n+1, m] - q[n, m-1]q[n, m+1]\end{aligned}\quad (15.14)$$

It has been shown that Ψ and Ψ^{2D} can intensify weak local anomalies of curvature mode shapes [19, 30]. Hence, it is proposed that the Ψ^{2D} be applied to $W''_{s,t}$ and $W_{s,t}^{(4)}$ for further intensifying local anomalies caused by damage and identifying its location: Teager energy of $W''_{s,t}$ (TE-CPFW) and that of $W_{s,t}^{(4)}$ (TE-C-CPFW) can be expressed by

$$\Psi^{2D}(W''_{s,t}[n, m]) = 2(W''_{s,t}[n, m])^2 - W''_{s,t}[n-1, m]W''_{s,t}[n+1, m] - W''_{s,t}[n, m-1]W''_{s,t}[n, m+1] \quad (15.15)$$

and

$$\begin{aligned}\Psi^{2D}(W_{s,t}^{(4)}[n, m]) &= 2(W_{s,t}^{(4)}[n, m])^2 - W_{s,t}^{(4)}[n-1, m]W_{s,t}^{(4)}[n+1, m] \\ &\quad - W_{s,t}^{(4)}[n, m-1]W_{s,t}^{(4)}[n, m+1]\end{aligned}\quad (15.16)$$

respectively, where $W''_{s,t}[n, m]$ and $W_{s,t}^{(4)}[n, m]$ denote the discrete values of $W''_{s,t}$ and $W_{s,t}^{(4)}$, respectively.

15.2.3 Damage Identification Based on Intensified Anomalies

When a mode shape is used for damage identification, it can be insensitive to certain damage or it cannot fully indicate the extent of the damage. In this case, uses of other mode shapes are necessary as the more mode shapes are used, the more likely the location and extent of the damage are identified. Similarly, not all waveforms and their associated anomalies described in Sect. 15.2.2 can fully indicate the location and extent of damage, and each of them may be able to indicate a fraction of the extent of the damage. While it is advantageous that a large number of waveforms are measured, an accumulative damage index that considers the local anomalies in Sect. 15.2.2, i.e., $W_{s,t}^{(4)}$, $\Psi^{2D}(W''_{s,t})$ and $\Psi^{2D}(W_{s,t}^{(4)})$, from available waveforms is proposed and expressed by

$$\delta(\Theta_t[n, m]) = \sum_{t=t_1}^{t=t_2} |\Theta_t[n, m]| \quad (15.17)$$

where $\Theta_t[n, m]$ denotes an intensified two-dimensional local anomaly, which can be $W_{s,t}^{(4)}$, $\Psi^{2D}(W''_{s,t})$ and $\Psi^{2D}(W_{s,t}^{(4)})$, t_1 and t_2 are the starting and ending instants of waveforms to be included in δ , and $|\cdot|$ denotes an absolute value.

While there are three anomalies to formulate δ in Eq. (15.17), the effectiveness of δ for identifying the location and extent of damage depends on values of t_1 and t_2 , which determine waveforms to be included. Since the use of waveforms near an excitation point can lead to misdiagnosis as local anomalies [23], t_1 should be selected as an instant after an excitation ends such that

$$t_1 > t_e \quad (15.18)$$

where t_e denotes the ending instant of the excitation. In this work, it is proposed that the proper value of t_1 be

$$t_1 = t_e + t_p \quad (15.19)$$

where t_p denotes the duration of the excitation. The inclusion of t_p in Eq. (15.19) can diminish misdiagnosis due to the waveforms generated during the occurrence of the excitation. Regarding the proper value of t_2 , it is proposed that the value be determined based on a convergence index, which is expressed by

$$\text{conv}(i) = \frac{\|\delta_i\|_2}{\|\delta_i\|_2 + \|\delta_i - \delta_{i+1}\|_2} \quad (15.20)$$

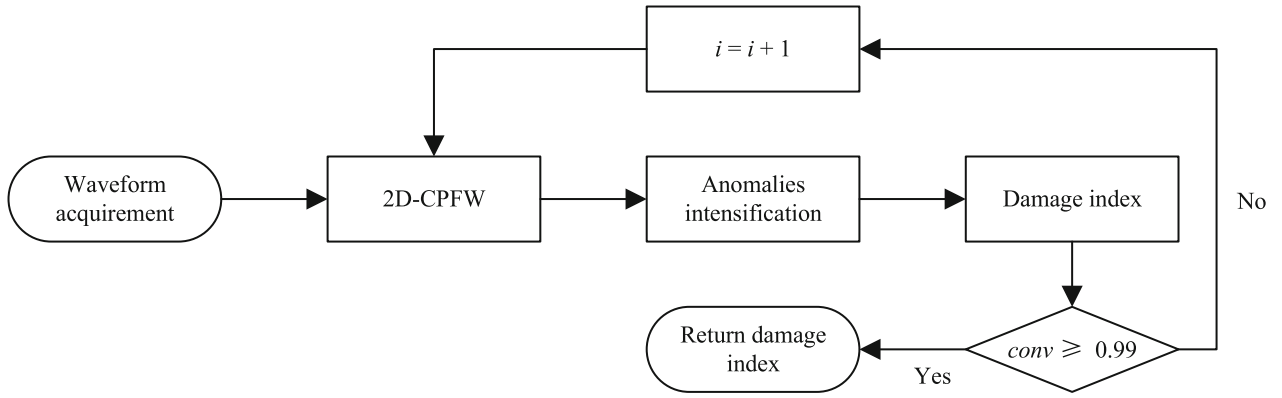


Fig. 15.1 Flowchart of the proposed damage identification method

where δ_i and δ_{i+1} are equal to δ in Eq. (15.17) with the same value of t_1 in Eq. (15.19) but different values of t_2 , and $\|\cdot\|_2$ denotes the 2-norm of a vector; the value of t_2 for δ_i in Eq. (15.20) is expressed by

$$t_2 = t_1 + \frac{ik}{f_s} \quad (15.21)$$

in which k denotes the number of waveforms for one increment in calculating $conv$ and f_s denotes the sampling frequency of the waveforms, and the value of t_2 in δ_{i+1} is expressed by

$$t_2 = t_1 + \frac{(i+1)k}{f_s} \quad (15.22)$$

As mentioned above, each waveform and its associated anomalies described in Sect. 15.2.2 can indicate a fraction of the extent of the damage. The damage index δ with a larger value of t_2 may lead to a more complete identification of the extent of the damage, since it cumulatively collects anomalies caused by the damage. Further, when t_2 is increased to a certain value, δ will converge and so will its identified extent. Hence, the index $conv$ quantifies the convergence of δ : when $conv = 1$, δ is considered convergent. Since a high sampling frequency is usually used to measure waveforms in practice, changes of δ between two consecutive sampling instants can be so small that a false convergence can be identified. And it can lead to a trivial $conv$ and inaccurate damage identification results. Hence, k is introduced to t_2 in Eq. (15.21) in order to include multiple waveforms to better quantify the convergence of δ . In this work, the proper value of t_2 is chosen as its minimum value, with which $conv \geq 0.99$. Finally, an auxiliary damage index is defined to further improve indication of the location and extent of the damage based on δ :

$$\tilde{\delta}(\Theta_t[n, m]) = \left(\frac{\delta(\Theta_t[n, m])}{\max(\delta(\Theta_t[n, m]))} \right)^2 \quad (15.23)$$

It is worth noted that $\tilde{\delta} \in [0, 1]$ and damage can be identified in neighborhoods with high $\tilde{\delta}$ values. A flowchart summarizing the proposed damage identification method is shown in Fig. 15.1.

15.3 Numerical Investigation

In this section, the effectiveness and noise-robustness of the proposed method are investigated using a numerical simulation of an aluminum plate with damage in the form of two thickness reduction areas.

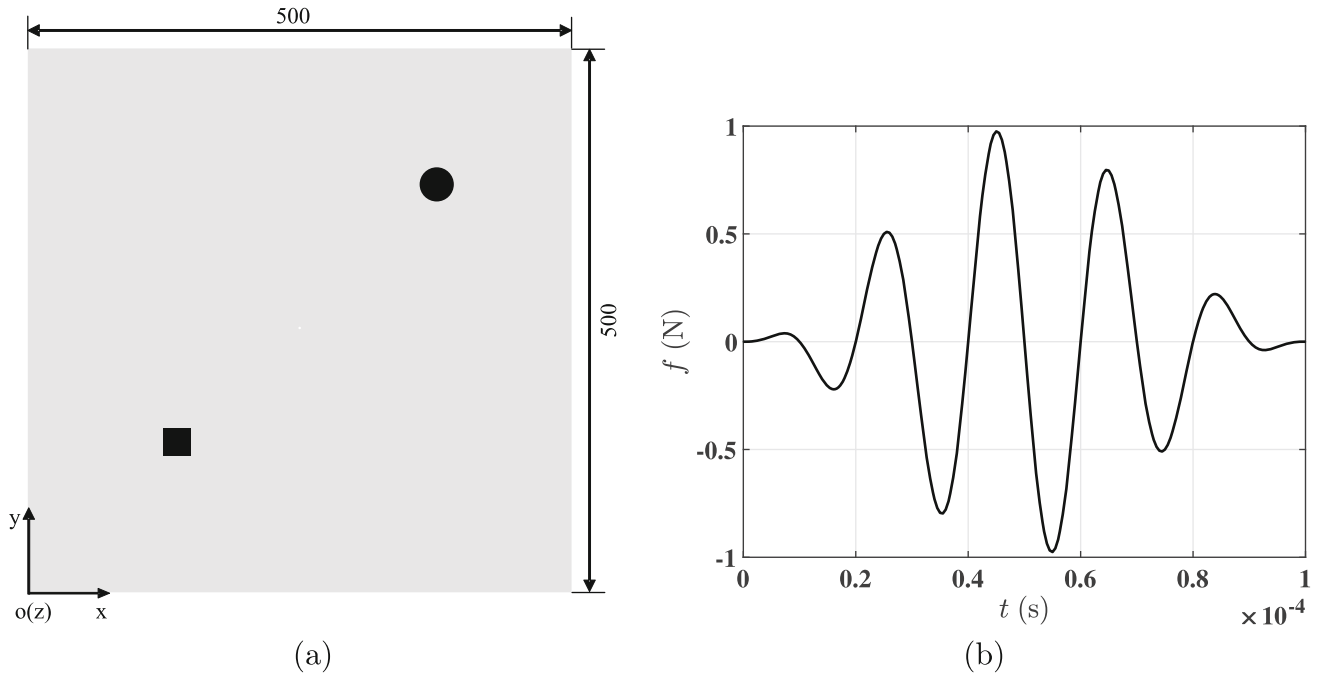


Fig. 15.2 (a) Dimensions of a damaged aluminum plate in the form of two thickness reduction areas (unit: mm) and (b) an excitation force in the form of a five-count wave packet. Locations and extent of square and circular damage areas are depicted by solid black areas in (a)

15.3.1 Numerical Test Specimen and Finite Element Model

A pinned-pinned-pinned-pinned aluminum plate of a length of 500 mm and a thickness 10 mm is modeled as a test specimen with dimensions shown in Fig. 15.2a. Its mass density is 2700 kg/m^3 , Young's modulus is 69 GPa, and Poisson's ratio is 0.33. A finite element model of the plate is constructed using ABAQUS with linear eight-node brick (C3D8R) elements. Two one-sided thickness reduction areas, including a square one and a circular one, with a depth of 5 mm are introduced. The square damage and circular damage area are centered at (137.5, 137.5) mm and (375, 375) mm, respectively; the square damage area has a side length of 25 mm and the circular damage area has a radius of $15\sqrt{2}$ mm. The damaged plate is under zero initial conditions and subject to an excitation force applied to its central location, i.e., (250, 250) mm. The excitation force is an N_c -count wave packet [8], which can be analytically expressed by

$$f(t) = A \left(H(t) - H\left(t - \frac{N_c}{f_c}\right) \right) \left(1 - \cos\left(\frac{2\pi f_c t}{N_c}\right) \right) \sin(2\pi f_c t) \quad (15.24)$$

where A denotes the amplitude of f , H is Heaviside function, which is expressed as

$$H(t) = \begin{cases} 1 & t \geq 0 \\ 0 & t < 0 \end{cases} \quad (15.25)$$

and f_c is the central frequency of the force. In this investigation, the applied excitation force is a five-count wave packet, as shown in Fig. 15.2b, with $A = 0.5 \text{ N}$, $N_c = 5$ and $f_c = 50 \text{ kHz}$.

Waveforms of propagating flexural waves of the damaged plate are obtained on a grid of 101×101 measurement points with a sampling frequency of 2 MHz for the first 500 μs after the excitation is applied; a total of 10001 waveforms are obtained. Figure 15.3a through d show four waveforms at 50 μs , 80 μs , 120 μs and 275 μs , respectively. In Fig. 15.3a, a propagating flexural wave is generated and spreads out from the excitation point, and its wavefront can be observed. In Fig. 15.3b, the wavefront of the propagating flexural wave is partially reflected near the top right corner of the square damage area. In Fig. 15.3c, the wavefront is beyond the square damage area and propagating flexural waves are partially reflected and scattered from the two damage areas. Subsequently, as shown in Fig. 15.3d, distinct wave propagation features related to the damage areas are not prominent, as they are masked by those related to reflections of the waves at the boundaries

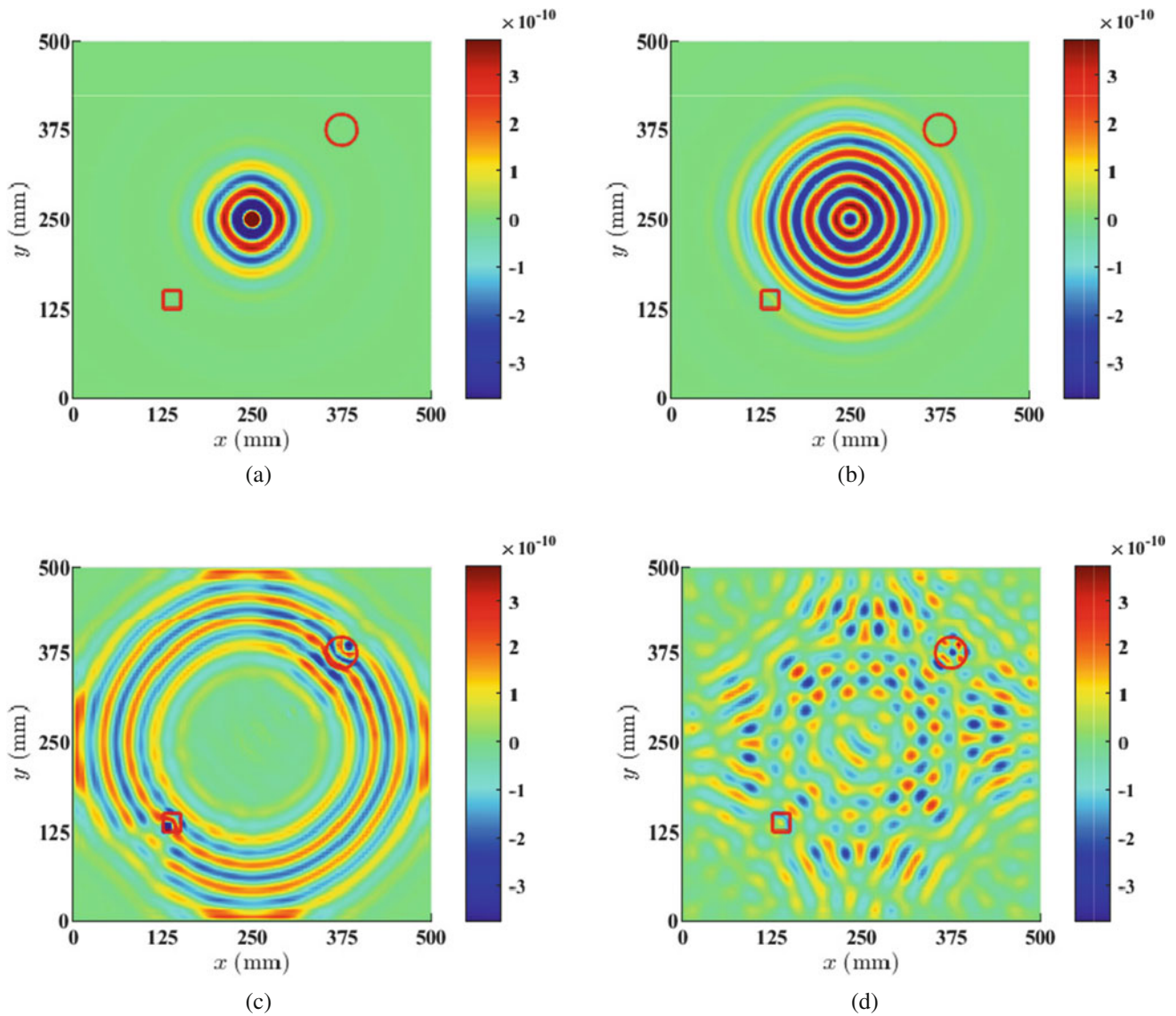


Fig. 15.3 Noise-free waveforms at (a) 50 μs , (b) 80 μs , (c) 120 μs , and (d) 275 μs . Locations and extent of square and circular damage areas are depicted by solid red lines

of the plate. To investigate effects of measurement noise on damage identification results, high-amplitude white Gaussian noise is added to the response of each measurement point of the damaged plate such that a signal-to-noise ratio (SNR) of -10 dB is achieved. Figure 15.4 shows the noise-contaminated waveforms at the instants same as those in Fig. 15.3. In Fig. 15.4, the overall propagation pattern of the noise-contaminated waves is similar to that of the noise-free ones, but the noise significantly impacts the waveforms. In Fig. 15.4a, the wavefront of the propagating flexural wave is blurred by the noise. In Fig. 15.4b, the reflected wave near the square damage area cannot be observed. In Fig. 15.4c, the reflected and scattered waves near the two damage areas can still be observed though the adverse effects of the noise are obvious. Subsequently, as shown in Fig. 15.4d, the distinct wave propagation features related to reflections at the boundaries are significantly masked by the noise.

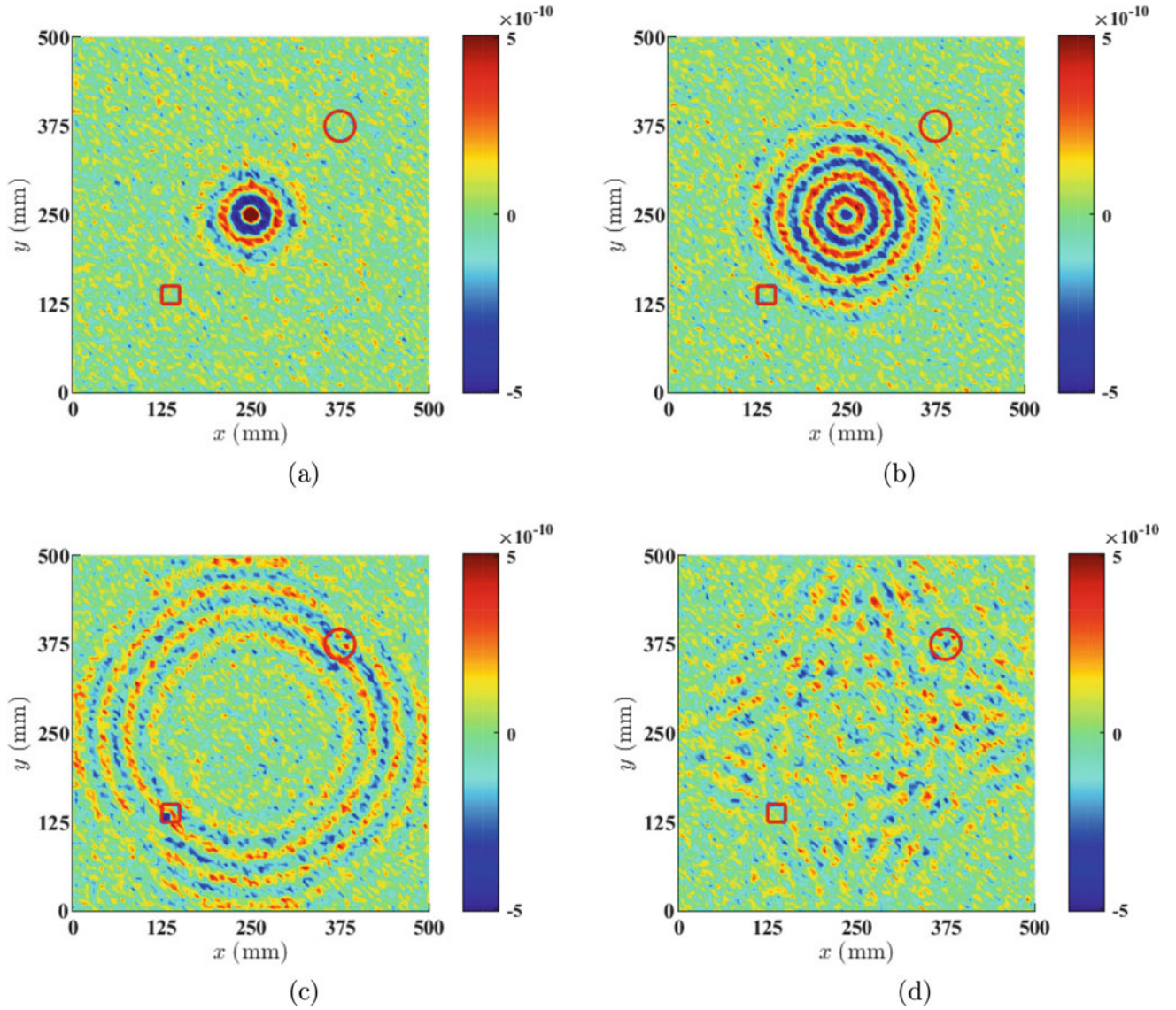


Fig. 15.4 Noise-contaminated waveforms at (a) 50 μs , (b) 80 μs , (c) 120 μs , and (d) 275 μs . Locations and extent of square and circular damage areas are depicted by solid red lines

15.3.2 Numerical Damage Identification Results and Discussion

The proposed damage identification method is applied to identify the damage on the plate. The use of the noise-free propagating flexural waves is first investigated. The convergence index $conv$ related to $W_{s,t}^{(4)}$, $\Psi^{2D}(W_{s,t}''')$, and $\Psi^{2D}(W_{s,t}^{(4)})$ are calculated and plotted in Fig. 15.5, where the values of t_1 in Eq. (15.19), k in Eq. (15.21) and s in Eq. (15.8) are selected to be 200 μs , 20 and 2, respectively. Base on $conv$, the values of t_2 corresponding to δ in Eq. (15.17) using $W_{s,t}^{(4)}$, $\Psi^{2D}(W_{s,t}''')$ and $\Psi^{2D}(W_{s,t}^{(4)})$ are selected to be 1310 μs , 960 μs , 780 μs , respectively.

Auxiliary damage index $\tilde{\delta}$ using $W_{s,t}^{(4)}$, $\Psi^{2D}(W_{s,t}''')$, and $\Psi^{2D}(W_{s,t}^{(4)})$ are calculated and shown in Fig. 15.6a, b and c, respectively. In Fig. 15.6a, large $\tilde{\delta}$ values are observed in the neighborhoods of the two damage areas, while smaller $\tilde{\delta}$ values are observed beyond the damage areas. Further, the size of the damage areas is well depicted by $\tilde{\delta}$ in Fig. 15.6a. Similar damage identification results can be observed in Fig. 15.6b and c. Specifically, as shown in Fig. 15.6d and e, relatively large values of $\tilde{\delta}$ using $\Psi^{2D}(W_{s,t}^{(4)})$ only exist within the damage areas, which is the same case for $\tilde{\delta}$ using $\Psi^{2D}(W_{s,t}''')$. Besides,

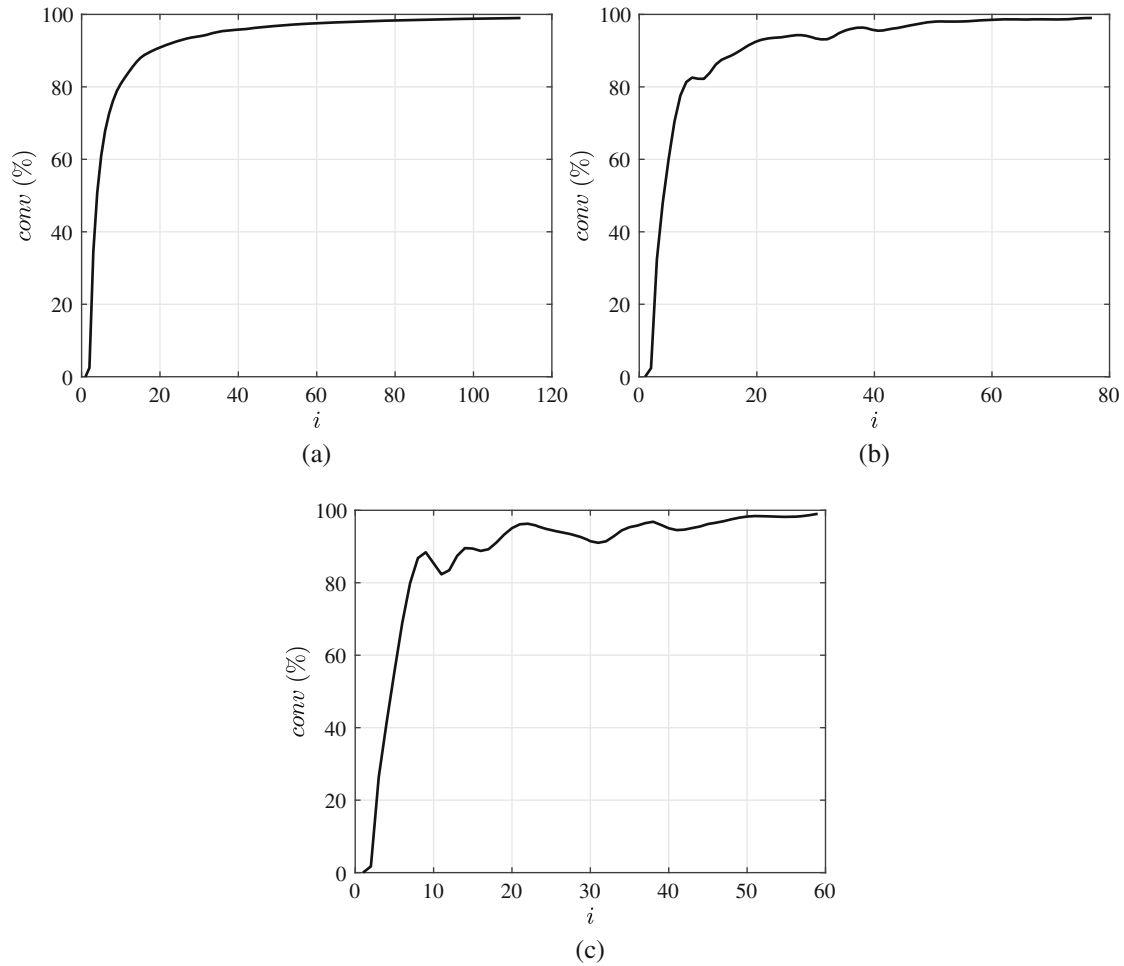


Fig. 15.5 Convergence indexes for the noise-free numerical propagating flexural waves based on (a) $W_{s,t}^{(4)}$ (b) $\Psi^{2D}(W_{s,t}'')$ and (c) $\Psi^{2D}(W_{s,t}^{(4)})$

smaller values of $\tilde{\delta}$ using $\Psi^{2D}(W_{s,t}'')$ and $\Psi^{2D}(W_{s,t}^{(4)})$ beyond the damage areas are observed, compared with those using $W_{s,t}^{(4)}$.

To study the noise-robustness of the proposed method, the use of the noise-contaminated propagating flexural waves is investigated. The proposed method is applied with the values of t_1 in Eq. (15.19), k in Eq. (15.21) and s in Eq. (15.8) are the same as those for the noise-free waveforms. The convergence indexes $conv$ related to $W_{s,t}^{(4)}$, $\Psi^{2D}(W_{s,t}'')$ and $\Psi^{2D}(W_{s,t}^{(4)})$ are calculated and plotted in Fig. 15.7. The values of t_2 corresponding to δ in Eq. (15.17) using $W_{s,t}^{(4)}$, $\Psi^{2D}(W_{s,t}'')$ and $\Psi^{2D}(W_{s,t}^{(4)})$ are selected to be 2140 μs , 1860 μs , 2100 μs , respectively. Compared with the values of t_2 for the noise-free waveforms, larger t_2 values are required for the noise-contaminated waveforms. Associated auxiliary damage index $\tilde{\delta}$ using $W_{s,t}^{(4)}$, $\Psi^{2D}(W_{s,t}'')$ and $\Psi^{2D}(W_{s,t}^{(4)})$ are calculated and plotted in Fig. 15.8a, b and c, respectively. In Fig. 15.8a, large $\tilde{\delta}$ values are observed in the neighborhoods of the two damage areas, while smaller $\tilde{\delta}$ values are observed beyond the damage areas. Similar results can be observed in Fig. 15.8b and c. Besides, smaller values of $\tilde{\delta}$ using $\Psi^{2D}(W_{s,t}'')$ and $\Psi^{2D}(W_{s,t}^{(4)})$ beyond the damage areas are observed, compared with those using $W_{s,t}^{(4)}$. It can be seen that $\tilde{\delta}$ using $\Psi^{2D}(W_{s,t}^{(4)})$ has the best performance for damage identification. The damage index $\tilde{\delta}$ using $\Psi^{2D}(W_{s,t}^{(4)})$ near the square and circular damage areas are zoomed and shown in Fig. 15.8d and e, respectively. It can be seen that relatively large $\tilde{\delta}$ values only exist within the damage areas.

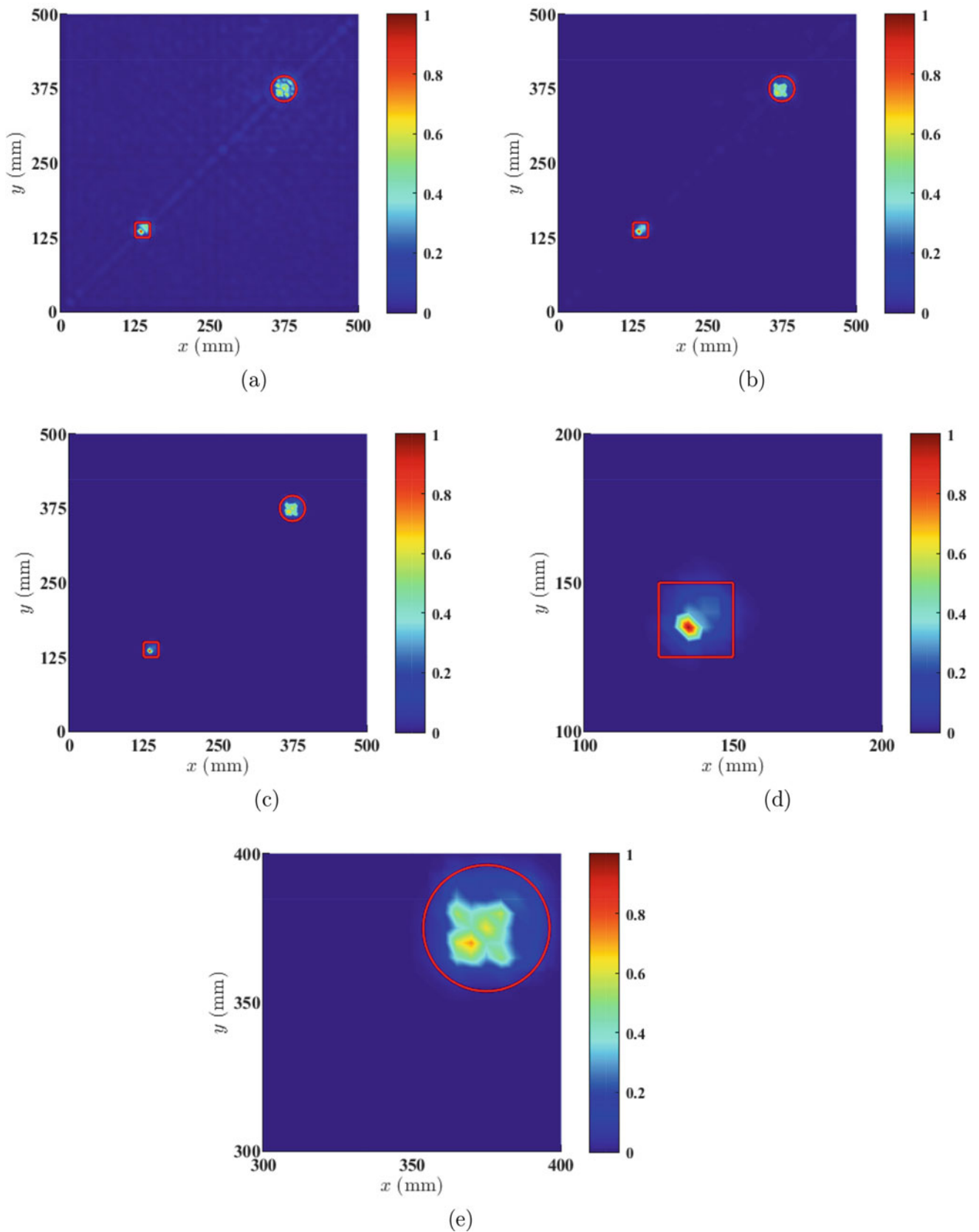


Fig. 15.6 Auxiliary damage index $\bar{\delta}$ for the noise-free numerical propagating flexural waves based on (a) $W_{s,t}^{(4)}$ (b) $\Psi^{2D}(W_{s,t}^{(4)})$, (c) $\Psi^{2D}(W_{s,t}^{(4)})$, (d) a zoomed-in view of the square damage area in (c) and (e) a zoomed-in view of the circular damage area in (c). Locations and extent of square and circular damage areas are depicted by solid red lines

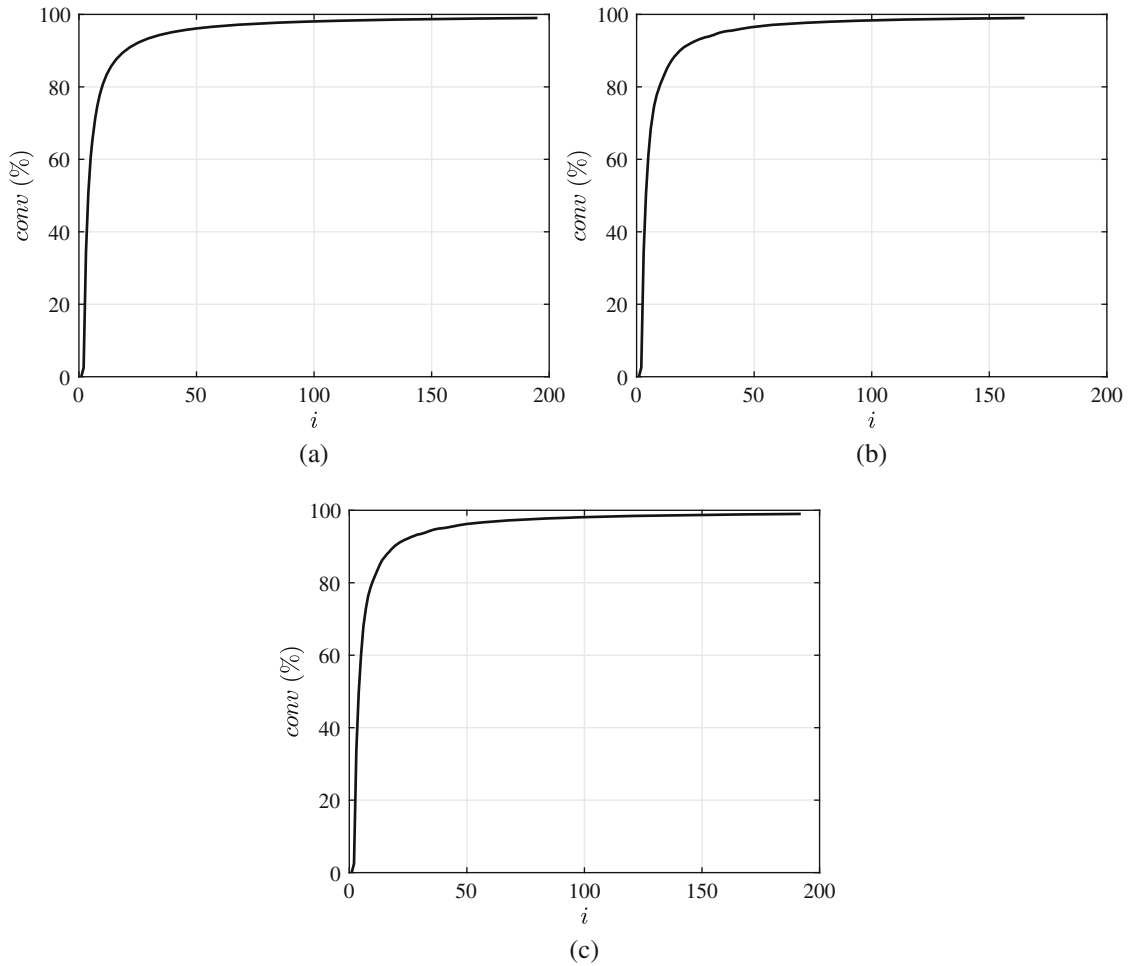


Fig. 15.7 Convergence indexes for the noise-contaminated numerical propagating flexural waves based on (a) $W_{s,t}^{(4)}$ (b) $\Psi^{2D}(W_{s,t}''')$ and (c) $\Psi^{2D}(W_{s,t}^{(4)})$

Effects of the scale parameter in CWT, i.e., s , on damage identification results using $\tilde{\delta}$ are studied in noise-contaminated propagating flexural waves. In this study, three other different s values are selected as 1, 3, and 4, respectively, to obtain $\tilde{\delta}$ values using $\Psi^{2D}(W_{s,t}^{(4)})$ and corresponding results are shown in Fig. 15.9a through c, respectively. It can be seen that all $\tilde{\delta}$ associated with these four different s values, i.e., 1 through 4, can indicate the location and extent of the damage. When increasing s from 1 to 2, smaller values of $\tilde{\delta}$ beyond the damage areas are observed. However, when increasing s from 2 to 3 relatively large values of $\tilde{\delta}$ beyond the damage areas are observed. The values of $\tilde{\delta}$ beyond the damage areas become larger when increasing s from 3 to 4. These observations indicate that the proposed method can identify the location and extent of the damage with high accuracy, the proposed method has high robustness against high-amplitude measurement noise in propagating flexural waves, and there exists an optimal s with which the location and extent of the damage can be identified with $\tilde{\delta}$, with whose values outside the damage areas are low.

15.4 Concluding Remarks

In this paper, a damage identification method is proposed for plate-like structures by extracting damage-induced local anomalies in waveforms of propagating flexural waves. In the proposed method, CWT with the second-order Gaussian function is used for calculating 2D-CPFW. Three types of local anomalies are intensified as the curvature of 2D-CPFW, TE-CPFW and TE-C-CPFW based on the 2D-CPFW. A damage index is proposed to identify damage based on these three

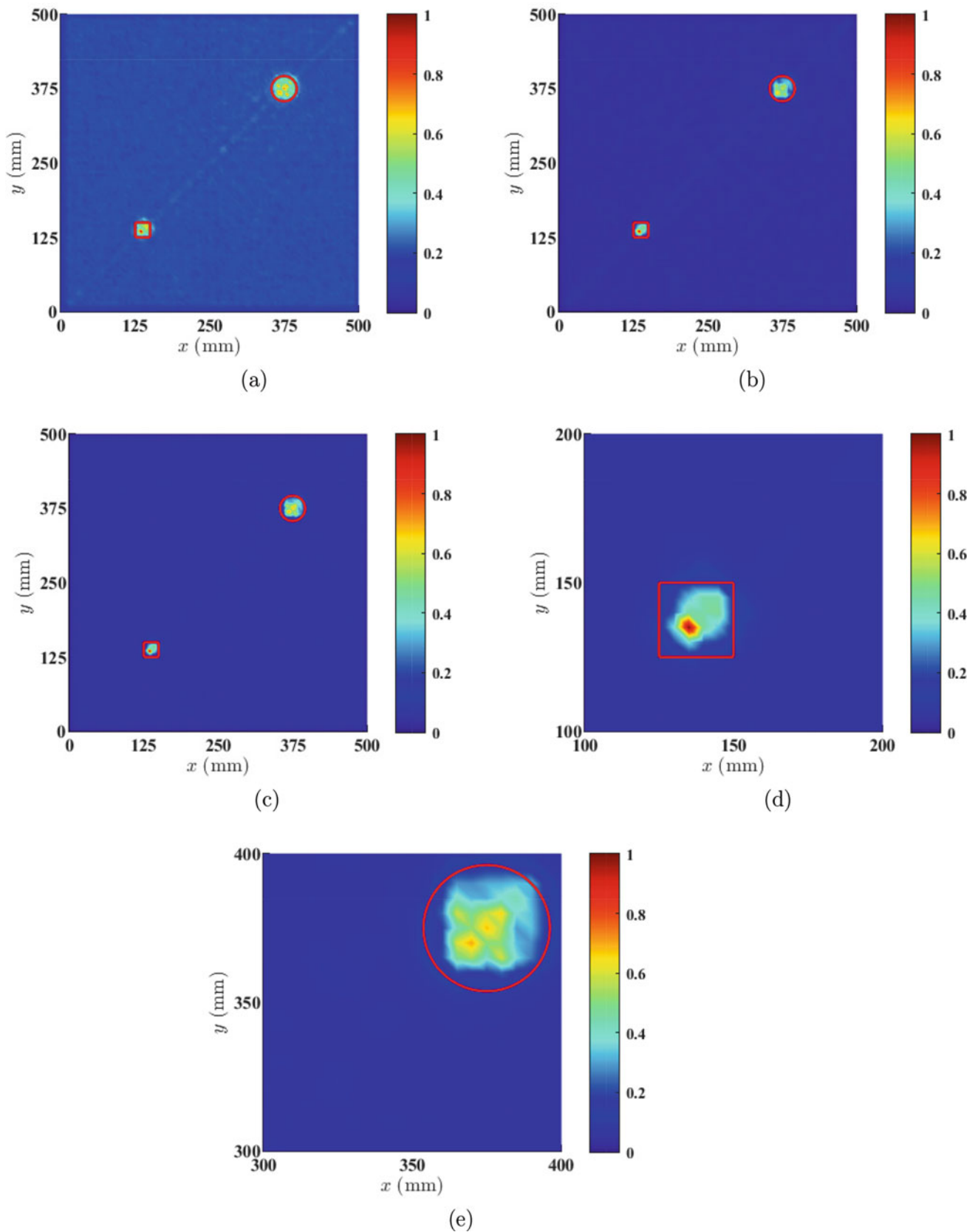


Fig. 15.8 Auxiliary damage index $\tilde{\delta}$ for the noise-contaminated numerical propagating flexural waves based on (a) $W_{s,t}^{(4)}$ (b) $\Psi^{2D}(W_{s,t}''')$, (c) $\Psi^{2D}(W_{s,t}^{(4)})$, (d) a zoomed-in view of the square damage area in (c) and (e) a zoomed-in view of the circular damage area in (c). Locations and extent of square and circular damage areas are depicted by solid red lines

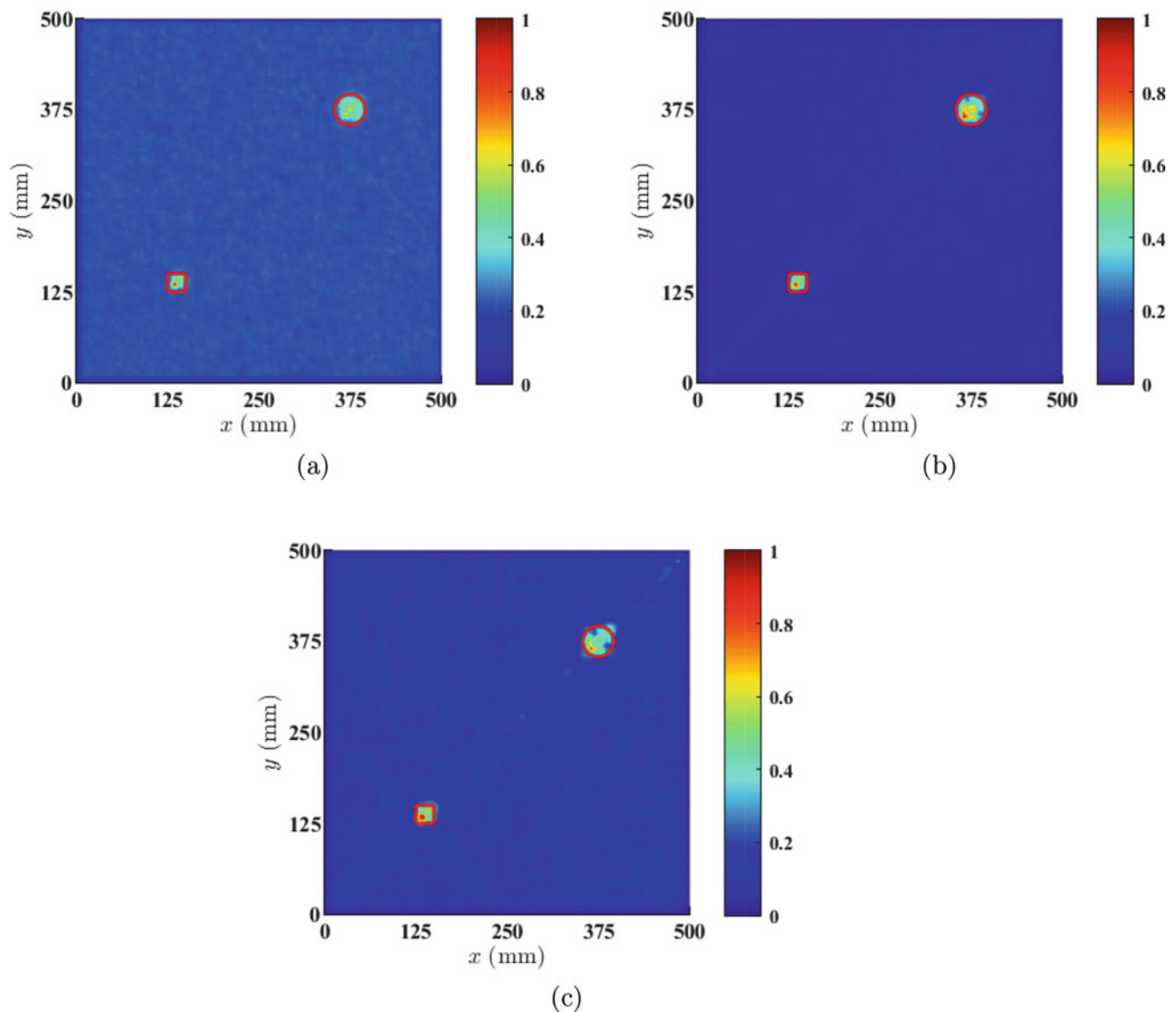


Fig. 15.9 Auxiliary damage index $\bar{\delta}$ for the noise-contaminated numerical propagating flexural waves based on $\Psi^{2D}(W_{s,t}^{(4)})$ with (a) $s = 1$, (b) $s = 3$ and (c) $s = 4$. Locations and extent of square and circular damage areas are depicted by solid red lines

types of local anomalies. When calculating the damage index, a convergence index is proposed to determine the number of included waveforms. The effectiveness of the proposed method is numerically investigated. It is found that the proposed method is accurate for identifying the location and extent of damage and robust against high-amplitude measurement noise.

Acknowledgments The authors are grateful for the financial support from the National Science Foundation through Grant No. CMMI-1762917.

Conflicts of Interest The authors declare no conflict of interest.

References

1. Bao, Y., Guo, Y., Li, H.: A machine learning–based approach for adaptive sparse time–frequency analysis used in structural health monitoring. *Struct. Health Monitor.* **19**(6), 1963–1975 (2020)
2. Smith, C.B., Hernandez, E.M.: Non-negative and sparsity constrained inverse problems in damage identification–application to a full-scale 3D truss. *Mech. Syst. Signal Process.* **140**, 106648 (2020)

3. Song, Y., Liu, Z., Rønnquist, A., Nāvīk, P., Liu, Z.: Contact wire irregularity stochastics and effect on high-speed railway pantograph–catenary interactions. *IEEE Trans. Instrum. Meas.* **69**(10), 8196–8206 (2020)
4. Fan, W., Qiao, P.: Vibration-based damage identification methods: a review and comparative study. *Struct. Health Monitor.* **10**(1), 83–111 (2011)
5. Padil, K.H., Bakhary, N., Abdulkareem, M., Li, J., Hao, H.: Non-probabilistic method to consider uncertainties in frequency response function for vibration-based damage detection using artificial neural network. *J. Sound Vibr.* **467**, 115069 (2020)
6. Huang, M.-S., Gül, M., Zhu, H.-P.: Vibration-based structural damage identification under varying temperature effects. *J. Aerosp. Eng.* **31**(3), 04018014 (2018)
7. Avci, O., Abdeljaber, O., Kiranyaz, S., Hussein, M., Gabbouj, M., Inman, D.J.: A review of vibration-based damage detection in civil structures: from traditional methods to machine learning and deep learning applications. *Mech. Syst. Signal Process.* **147**, 107077 (2021)
8. Xu, Y., Kim, J.: Baseline-free structural damage identification for beam-like structures using curvature waveforms of propagating flexural waves. *Sensors* **21**(7), 2453 (2021)
9. Adams, R., Walton, D., Flitcroft, J., Short, D.: *Vibration Testing as a Nondestructive Test Tool for Composite Materials*. Composite Reliability. ASTM International, West Conshohocken (1975)
10. Adams, R., Cawley, P., Pye, C., Stone, B.: A vibration technique for non-destructively assessing the integrity of structures, *J. Mech. Eng. Sci.* **20**(2), 93–100 (1978)
11. Hu, H., B.-T. Wang, C.-H. Lee, J.-S. Su: Damage detection of surface cracks in composite laminates using modal analysis and strain energy method. *Composite Struct.* **74**(4), 399–405 (2006)
12. Pandey, A., Biswas, M., Samman, M.: Damage detection from changes in curvature mode shapes. *J. Sound Vibr.* **145**(2), 321–332 (1991)
13. Ratcliffe, C.P.: A frequency and curvature based experimental method for locating damage in structures. *ASME J. Vibr. Acoust.* **122**(3), 324–329 (2000)
14. Rucka, M., Wilde, K.: Application of continuous wavelet transform in vibration based damage detection method for beams and plates. *J. Sound Vibr.* **297**(3–5), 536–550 (2006)
15. Xu, W., Radzieński, M., Ostachowicz, W., Cao, M.: Damage detection in plates using two-dimensional directional gaussian wavelets and laser scanned operating deflection shapes. *Struct. Health Monitor.* **12**(5–6), 457–468 (2013)
16. Cao, M., Xu, W., Ostachowicz, W., Su, Z.: Damage identification for beams in noisy conditions based on Teager energy operator-wavelet transform modal curvature. *J. Sound Vibr.* **333**(6), 1543–1553 (2014)
17. Xu, W., Ding, K., Liu, J., Cao, M., Radzieński, M., Ostachowicz, W.: Non-uniform crack identification in plate-like structures using wavelet 2D modal curvature under noisy conditions. *Mech. Syst. Signal Process.* **126**, 469–489 (2019)
18. Cao, M., Radzieński, M., Xu, W., Ostachowicz, W.: Identification of multiple damage in beams based on robust curvature mode shapes. *Mech. Syst. Signal Process.* **46**(2), 468–480 (2014)
19. Xu, W., Cao, M., Ostachowicz, W., Radzieński, M., Xia, N.: Two-dimensional curvature mode shape method based on wavelets and Teager energy for damage detection in plates. *J. Sound Vibr.* **347**, 266–278 (2015)
20. Ruzzene, M.: Frequency-wavenumber domain filtering for improved damage visualization. In: *Ultrasonic and Advanced Methods for Nondestructive Testing and Material Characterization*, pp. 591–611. World Scientific, Singapore (2007)
21. Kudela, P., Radzieński, M., Ostachowicz, W.: Identification of cracks in thin-walled structures by means of wavenumber filtering. *Mech. Syst. Signal Process.* **50**, 456–466 (2015)
22. Yu, L., Tian, Z.: Lamb wave structural health monitoring using a hybrid pzt-laser vibrometer approach. *Struct. Health Monitor.* **12**(5–6), 469–483 (2013)
23. Ruzzene, M., Jeong, S., Michaels, T., Michaels, J., Mi, B.: Simulation and measurement of ultrasonic waves in elastic plates using laser vibrometry. In: *AIP Conference Proceedings*, vol. 760, pp. 172–179. American Institute of Physics, College Park (2005)
24. Żak, A., Radzieński, M., Krawczuk, M., Ostachowicz, W.: Damage detection strategies based on propagation of guided elastic waves. *Smart Mater. Struct.* **21**(3), 035024 (2012)
25. Sha, G., Xu, H., Radzieński, M., Cao, M., Ostachowicz, W., Su, Z.: Guided wavefield curvature imaging of invisible damage in composite structures. *Mech. Syst. Signal Process.* **150**, 107240 (2021)
26. Yoon, M., Heider, D., Gillespie Jr, J., Ratcliffe, C., Crane, R.: Local damage detection using the two-dimensional gapped smoothing method. *J. Sound Vibr.* **279**(1–2), 119–139 (2005)
27. Mallat, S.: *A Wavelet Tour of Signal Processing*. Elsevier, Amsterdam (1999)
28. Xu, Y., Zhu, W., Liu, J., Shao, Y.: Identification of embedded horizontal cracks in beams using measured mode shapes. *J. Sound Vibr.* **333**(23), 6273–6294 (2014)
29. Xu, Y., Zhu, W.: Non-model-based damage identification of plates using measured mode shapes. *Struct. Health Monitor.* **16**(1), 3–23 (2017)
30. Xu, W., Zhu, W., Xu, Y., Cao, M.: A comparative study on structural damage detection using derivatives of laser-measured flexural and longitudinal vibration shapes. *J. Nondestr. Eval.* **39**(3), 1–17 (2020)
31. Rucka, M.: Damage detection in beams using wavelet transform on higher vibration modes. *J. Theor. Appl. Mech.* **49**(2), 399–417 (2011)
32. Kaiser, J.F.: On a simple algorithm to calculate the ‘energy’ of a signal. In: *International Conference on Acoustics, Speech, and Signal Processing*, pp. 381–384. IEEE, Piscataway (1990)
33. Boudraa, A.-O., Diop, E.-H.S.: Image contrast enhancement based on 2D Teager-Kaiser operator. In: *2008 15th IEEE International Conference on Image Processing*, pp. 3180–3183. IEEE, Piscataway (2008)